

# An in-medium full-folding model approach to quasielastic (p,n) charge-exchange reactions

H. F. Arellano\*

*Department of Physics - FCFM, University of Chile  
Av. Blanco Encalada 2008, Santiago, Chile*

W. G. Love†

*Department of Physics and Astronomy,  
University of Georgia, Athens, GA-30602, U.S.A.*

(Dated: February 1, 2008)

## Abstract

A microscopic description of the quasielastic ( $p,n$ ) charge-exchange reaction (here, charge-exchange scattering between analogue states) is presented and discussed. Emphasis is focused on the spin-isospin structure of the projectile-target coupling. The model is a coupled-channel extension of the full-folding optical model approach (OMP) developed for nucleon elastic scattering, where emphasis is placed on retaining the genuine off-shell behavior of realistic effective interactions in the nuclear medium. The resulting non-local optical potentials are applied to the calculation of ( $p,n$ ) differential cross sections, with particular emphasis on small-angle Fermi ( $\Delta S = 0$ ) cross-sections to isobaric analog states. These parameter-free results provide a reasonable description of the  $^{14}\text{C}(p,n)$ -data at proton energies above  $\sim 100$  MeV, but deteriorate for heavier targets. These shortcomings are analyzed and possible ways to correct them are discussed.

PACS numbers: 24.10.Eq, 24.10.Ht, 25.40.Kv,

---

\*Electronic address: arellano@dfi.uchile.cl; URL: <http://www.omp-online.cl>

†Electronic address: wglove@physast.uga.edu

## I. INTRODUCTION

An issue of high current interest in nuclear research is the physics behind systems and processes where the isovector component of the nuclear interaction is relevant. This particular aspect is of pivotal importance in understanding a wide variety of phenomena such as extreme isospin asymmetric nuclear matter, nuclear systems far from stability, collisions of radioactive beams, the asymmetry energy of nuclear systems and  $(p,n)$  charge-exchange processes [1, 2, 3, 4, 5, 6]. A sound understanding of these phenomena may have significant impact on other areas of research such the physics of neutron stars, the formation of astrophysical objects, etc. Our focus here is on the study of charge-exchange reactions at intermediate energies. This effort attempts to provide a rigorous microscopic approach for the study of these reactions with emphasis on a detailed account of genuine energy, momentum and density effects in the nucleon-nucleon ( $NN$ ) effective interaction.

The study of  $(p,n)$  charge-exchange reactions at intermediate energies has received considerable attention during the past few decades. These reactions have been of great value in understanding the isovector modes of excitation of nuclei. At beam energies above 100 MeV, nucleon charge-exchange reactions can be considered as a one step process, thus allowing a rather clean separation of the nuclear structure from the underlying  $NN$  effective interaction. These arguments have resulted in the usual  $t\rho$  structure of the coupling to the nucleus. Furthermore, the weak strength of the isovector component of the interaction relative to its isoscalar counterpart has made suitable the use of the distorted wave Born approximation (DWBA). In spite of these advantageous considerations, no microscopic effort has been able to satisfactorily describe the differential cross-section data without phenomenological adjustments *a posteriori* of the nucleon-nucleus ( $NA$ ) coupling. This impediment is quite significant in that it points to a lack of understanding of the simplest process beyond elastic collisions. Therefore, a comprehensive and consistent re-analysis of the problem is relevant.

Studies of nucleon elastic scattering at intermediate energies (i.e. between 100 MeV and 1 GeV) have demonstrated the importance of off-shell effects as accounted for within the full-folding OMP for ( $NA$ ) scattering. In particular, it was shown that the  $t\rho$  scheme (as most often applied) is insufficient to satisfactorily describe intermediate energy data. Furthermore, nuclear medium effects as included by using nuclear matter  $g$  matrices have provided significant improvements in the description of the elastic scattering data [7, 8, 9].

The issue which naturally arises is whether these improvements within the full-folding OMP to  $NA$  elastic scattering are also important in charge-exchange processes.

Although significant advances have been made with the introduction of full-folding optical potentials in the description of nucleon elastic scattering, none of these improvements have been included in charge-exchange reactions [10]. Furthermore, most of the reported  $(p,n)$  reaction calculations, which provide a reasonable description of the data, are semi-phenomenological in the sense that well fitted potentials in the elastic channel are used to obtain the charge-exchange cross-section by means of the DWBA [11, 12]. From this prospective additional theoretical effort is needed to clarify the issues which prevent us from obtaining a unified understanding of these phenomena. Along this line, the aim of the present work is to assess the importance of treating the intrinsic off-shell behavior of, and medium corrections to, realistic nuclear effective interactions in the calculation of nuclear charge-exchange reactions. For this purpose we present the spin-isospin formalism needed to calculate these couplings within the non-local full-folding optical model and have developed the required coupled-channel scattering codes to solve the scattering problem exactly. Our work is focused on the  $\Delta S = 0$  isobaric analog state (IAS) transitions for various targets and incident proton energies.

We organize this article in five sections as follows. In Section II we review the spin-isospin structure of the  $NA$  coupling to display its formal structure suited for charge-exchange reactions from a finite nucleus. In Section III we outline the coupled-channel approach for studying the  $(p,n)$  charge-exchange reactions with non-local potentials in the presence of the Coulomb interaction. In Section IV we present and interpret results for representative applications and in Section V we summarize the present work and draw the main conclusions.

## II. OPTICAL POTENTIAL: SPIN AND ISOSPIN CONSIDERATIONS

For simplicity in this discussion, we use the free  $t$  matrix as the  $NN$  effective interaction and consider nonrelativistic kinematics. Both of these restrictions will be removed in the following sections. Thus, the generalized optical potential for nucleon scattering and charge-

exchange reactions may be written in momentum space as

$$\begin{aligned} \langle \mathbf{k}' \nu' \mu' | U | \mathbf{k} \nu \mu \rangle = & \sum_{m, m', n, n'} \iint d\mathbf{p}' d\mathbf{p} \langle F | \psi_{\frac{1}{2}m', \frac{1}{2}n'}^\dagger(\mathbf{p}') \bar{\psi}_{\frac{1}{2}m, \frac{1}{2}n}(\mathbf{p}) | I \rangle \\ & \langle \mathbf{p}' m' n', \mathbf{k}' \nu' \mu' | t | \mathbf{p} m n, \mathbf{k} \nu \mu \rangle_A. \end{aligned} \quad (1)$$

Here  $\langle t \rangle_A$  is the antisymmetrized  $NN$   $t$  matrix;  $\nu$  and  $\mu$  denote the initial spin and isospin projections of the projectile and

$$\bar{\psi}_{\frac{1}{2}m, \frac{1}{2}n}(\mathbf{p}) = (-)^{\frac{1}{2}-m+\frac{1}{2}-n} \psi_{\frac{1}{2}-m, \frac{1}{2}-n}(\mathbf{p})$$

where  $\psi_{\frac{1}{2}-m, \frac{1}{2}-n}(\mathbf{p})$  annihilates a nucleon with momentum  $\mathbf{p}$  and spin and isospin projections  $-m$  and  $-n$ , respectively. The choice of the pair  $(\mu, \mu')$  is determined by the reaction being considered. In the convention in which the proton has isospin projection  $+\frac{1}{2}$ ,

$$(\mu, \mu') = (\frac{1}{2}, \frac{1}{2}), (\frac{1}{2}, -\frac{1}{2}), (-\frac{1}{2}, \frac{1}{2}), (-\frac{1}{2}, -\frac{1}{2})$$

for the  $(p, p)$ ,  $(p, n)$ ,  $(n, p)$ , and  $(n, n)$  reactions, respectively. Following some recoupling to display the transferred quanta and the  $NN$  spin and isospin,  $U$  becomes:

$$\begin{aligned} U(S_t = 0, T_t = T_p) = & \frac{1}{4} \sum_{S_p, T_p} \langle \nu' | \mathbb{S}(S_p, -\nu_p) | \nu \rangle \langle \mu' | \mathbb{T}(T_p, -n_t) | \mu \rangle (-)^{n_t} \\ & \iint d\mathbf{p} d\mathbf{p}' \langle F | [\psi_{\frac{1}{2}\frac{1}{2}}^\dagger(\mathbf{p}') \otimes \bar{\psi}_{\frac{1}{2}\frac{1}{2}}(\mathbf{p})]^{00; T_p n_t} | I \rangle \\ & \sum_{S, T, M, M'} \langle S S_p M - \nu_p | S M' \rangle (-)^{1-T} (2T+1) \\ & W(\frac{1}{2}\frac{1}{2}\frac{1}{2}\frac{1}{2}; T_p T) \langle \mathbf{p}' \mathbf{k}', S M', T | t | \mathbf{p} \mathbf{k}, S M, T \rangle_A, \end{aligned} \quad (2)$$

where

$$[\psi_{\frac{1}{2}\frac{1}{2}}^\dagger(\mathbf{p}') \otimes \bar{\psi}_{\frac{1}{2}\frac{1}{2}}(\mathbf{p})]^{SM; TN} = \sum_{m, m', n, n'} \langle \frac{1}{2}m' \frac{1}{2}m | SM \rangle \langle \frac{1}{2}n' \frac{1}{2}n | TN \rangle \psi_{\frac{1}{2}m', \frac{1}{2}n'}^\dagger(\mathbf{p}') \bar{\psi}_{\frac{1}{2}m, \frac{1}{2}n}(\mathbf{p}), \quad (3)$$

defines the order of coupling.  $T_p$  and  $T_t$  denote the isospin transfers to the projectile and target, respectively. Similarly,  $S_p$  and  $S_t$  denote the corresponding spin transfers. Also,

$$\mathbb{S}(0, 0) = 1, \quad \mathbb{S}(1, -\nu_p) = \sigma_{-\nu_p}, \quad \mathbb{T}(0, 0) = 1, \quad \mathbb{T}(1, -n_t) = \tau_{-n_t},$$

where  $\sigma_{-\nu_p}$  ( $\tau_{-n_t}$ ) is the  $-\nu_p$  ( $-n_t$ ) spherical component of the Pauli spin (isospin) matrix. The sum over  $M, M'$  projects out that part of the  $t$  matrix which acts in the spin state  $S$

and which is of rank  $S_p$  in spin space. In particular, we write the  $t$  matrix as a sum over the contributing ranks  $(\lambda)$  in spin space

$$t = \sum_{\lambda=0}^2 \sum_{S,T} t_{ST}^{(\lambda)} \cdot O_S^{(\lambda)} \mathcal{P}_T, \quad (4)$$

where

$$O_S^{(\lambda)} = \mathcal{P}_S \delta_{\lambda 0} + (\vec{\sigma}_1 + \vec{\sigma}_2) \delta_{S1} \delta_{\lambda 1} + (\vec{\sigma}_1 \otimes \vec{\sigma}_2)^2 \delta_{S1} \delta_{\lambda 2}. \quad (5)$$

Here,  $\mathcal{P}_S$  and  $\mathcal{P}_T$  are the projection operators onto the  $NN$  states of spin  $S$  and isospin  $T$ , respectively. The optical potential  $U$  corresponding to zero spin transfer to the target and  $T_t = T_p$  isospin transfer to the target and projectile becomes:

$$U = \sum_{S_p, T_p} \iint d\mathbf{p} d\mathbf{p}' \rho_{FI}^{T_t}(\mathbf{p}', \mathbf{p}) \cdot \langle \mu' | \mathbb{T}(T_p, \mu' - \mu) | \mu \rangle \frac{\langle \nu' | \mathbb{S}(S_p, \nu' - \nu) | \nu \rangle}{2S_p + 1} \\ \frac{1}{8} \sum_{S, T} (-)^{1-T} (2T + 1)(2S + 1) W(\frac{1}{2} \frac{1}{2} \frac{1}{2} \frac{1}{2}; T_t T) \langle \mathbf{p}' \mathbf{k}' | t_{ST}^{(S_p)} | \mathbf{p} \mathbf{k} \rangle_A. \quad (6)$$

The nuclear structure is contained in the mixed transition density defined by

$$\rho_{FI}^{T_t}(\mathbf{p}', \mathbf{p}) = 2 \langle F | [\psi_{\frac{1}{2}\frac{1}{2}}^\dagger(\mathbf{p}') \otimes \bar{\psi}_{\frac{1}{2}\frac{1}{2}}(\mathbf{p})]^{00; T_t} | I \rangle, \quad (7)$$

which is an isoscalar or isovector as  $T_p = T_t$  is 0 or 1. With this normalization for  $\rho_{FI}^{T_t}$ ,  $\int d\mathbf{p} \rho_{II}^0(\mathbf{p}, \mathbf{p}) = A$ , the number of nucleons in state  $I$ . In the evaluation of the optical potential it is useful to make explicit use of the translational invariance characteristic of the free  $NN$  interaction (or that in infinite nuclear matter) by writing it as

$$\langle \mathbf{p}' \mathbf{k}' | t_{ST}^{(S_p)} | \mathbf{p} \mathbf{k} \rangle_A = \delta(\mathbf{p} + \mathbf{k} - \mathbf{p}' - \mathbf{k}') \langle \boldsymbol{\kappa}' | t_{ST}^{(S_p)} | \boldsymbol{\kappa} \rangle_A, \quad (8)$$

where the relative momenta  $\boldsymbol{\kappa}$  and  $\boldsymbol{\kappa}'$  are given by:

$$\boldsymbol{\kappa} = \frac{\mathbf{p} - \mathbf{k}}{2}, \quad \boldsymbol{\kappa}' = \frac{\mathbf{p}' - \mathbf{k}'}{2}. \quad (9)$$

For brevity, it is also convenient to introduce the participating part of the  $NN$  interaction from Eq. (6) as

$$\langle \boldsymbol{\kappa}' | \mathbf{t}^{S_p T_t} | \boldsymbol{\kappa} \rangle_A = \frac{1}{8} \sum_{S, T} (-)^{1+T} (2T + 1)(2S + 1) W(\frac{1}{2} \frac{1}{2} \frac{1}{2} \frac{1}{2}; T_t T) \langle \boldsymbol{\kappa}' | t_{ST}^{(S_p)} | \boldsymbol{\kappa} \rangle_A, \quad (10)$$

where  $W$  is the usual Racah coefficient,

$$W(\frac{1}{2} \frac{1}{2} \frac{1}{2} \frac{1}{2}; T_t T) = \begin{pmatrix} -\frac{1}{2} & \frac{1}{2} \\ \frac{1}{2} & \frac{1}{6} \end{pmatrix},$$

and  $S_t = 0$  for the optical potential.

### A. Scattering from a Fermi Gas ( $N \geq Z$ ): an example

For elastic nucleon scattering, the transition density of Eq. (7) becomes

$$\rho_{FI}^{T_t}(\mathbf{p}', \mathbf{p}) = 2 \delta(\mathbf{p}' - \mathbf{p}) [\Theta(p_F(\pi) - p) + (-)^{T_t} \Theta(p_F(\nu) - p)] , \quad (11)$$

where  $\Theta(x)$  is the Heaviside step function and  $p_F(\pi)$  and  $p_F(\nu)$  denote the Fermi momenta for protons and neutrons, respectively. The transition density appropriate for the excitation of the analogue state *via* the charge-exchange reaction is

$$\rho_{FI}^{T_t}(\mathbf{p}', \mathbf{p}) = 2 \sqrt{\frac{2}{N-Z}} \delta(\mathbf{p}' - \mathbf{p}) [\Theta(p_F(\nu) - p) - \Theta(p_F(\pi) - p)] , \quad (12)$$

where  $|F\rangle$  satisfies

$$|F\rangle = \frac{1}{\sqrt{N-Z}} T_+ |I\rangle .$$

In the Fermi gas (FG) approximation we must have from Eqs. (8,9,11),  $\mathbf{p} = \mathbf{p}'$ ,  $\mathbf{k} = \mathbf{k}'$  and therefore  $\boldsymbol{\kappa} = \boldsymbol{\kappa}'$ . This insures that only the  $S_p = 0$  part of the  $t$  matrix participates as the spin-orbit and tensor terms do not contribute to forward scattering in the  $NN$  system. With these observations, the optical potential for elastic scattering given by Eq. (6) becomes

$$U_{FG} = 2 \delta_{\mu,\mu'} \delta_{\nu,\nu'} \delta(\mathbf{k} - \mathbf{k}') \int d\mathbf{p} \left\{ \Theta[p_F(l) - p] \langle \boldsymbol{\kappa} | \mathbf{t}^0 + \mathbf{t}^1 | \boldsymbol{\kappa} \rangle_A + \Theta[p_F(u) - p] \langle \boldsymbol{\kappa} | \mathbf{t}^0 - \mathbf{t}^1 | \boldsymbol{\kappa} \rangle_A \right\} , \quad (13)$$

where  $l$  ( $u$ ) denotes target nucleons like (unlike) the projectile; e.g. for proton scattering,  $l$  corresponds to target protons and  $u$  to target neutrons. Also, we have dropped the  $S_p = 0$  superscript on the reduced  $t$  matrix  $\mathbf{t}^{T_t}$ . Separating the isoscalar and isovector contributions to Eq. (13) gives

$$\begin{aligned} U_{FG} = 2 \delta_{\mu,\mu'} \delta_{\nu,\nu'} \delta(\mathbf{k} - \mathbf{k}') \times \\ \int d\mathbf{p} \left( \{ \Theta[p_F(l) - p] + \Theta[p_F(u) - p] \} \langle \boldsymbol{\kappa} | \mathbf{t}^0 | \boldsymbol{\kappa} \rangle_A \right. \\ \left. + \{ \Theta[p_F(l) - p] - \Theta[p_F(u) - p] \} \langle \boldsymbol{\kappa} | \mathbf{t}^1 | \boldsymbol{\kappa} \rangle_A \right) . \end{aligned} \quad (14)$$

For the nucleon charge-exchange reaction exciting the isobaric analogue state, the Fermi gas transition potential is

$$\begin{aligned} U_{FG} = \frac{-4}{\sqrt{N-Z}} \delta_{\mu',\mu-1} \delta_{\nu,\nu'} \delta(\mathbf{k} - \mathbf{k}') \\ \int d\mathbf{p} \{ \Theta[p_F(\nu) - p] - \Theta[p_F(\pi) - p] \} \langle \boldsymbol{\kappa} | \mathbf{t}^1 | \boldsymbol{\kappa} \rangle_A . \end{aligned} \quad (15)$$

Some insight into the relationship of the optical model in the Fermi gas to that in finite nuclei may be obtained by using the Fourier representation of the momentum-conserving delta function appearing as a factor in  $U_{FG}$  above, e.g.

$$\delta(\mathbf{k} - \mathbf{k}') = \frac{1}{(2\pi)^3} \int d\mathbf{r} e^{i(\mathbf{k}-\mathbf{k}')\cdot\mathbf{r}},$$

together with the assumption that the  $t$  matrix varies little over the range of  $p$  allowed by the Fermi momentum. When this is done, the integrals over the step functions may be done giving

$$\frac{4\pi}{3} p_F^3 = 4\pi^3 \rho,$$

for protons ( $\pi$ ) and neutrons ( $\nu$ ), and the optical potential for elastic scattering becomes

$$U_{FG} = \delta_{\mu,\mu'} \delta_{\nu,\nu'} \int d\mathbf{r} e^{i(\mathbf{k}-\mathbf{k}')\cdot\mathbf{r}} ( \rho_l \langle \boldsymbol{\kappa} | \mathbf{t}^0 + \mathbf{t}^1 | \boldsymbol{\kappa} \rangle_A + \rho_u \langle \boldsymbol{\kappa} | \mathbf{t}^0 - \mathbf{t}^1 | \boldsymbol{\kappa} \rangle_A ), \quad (16)$$

where  $\boldsymbol{\kappa}$  is to be evaluated at  $p = 0$ , for example. In the strict Fermi gas model only the exponential above depends on  $\mathbf{r}$  and we recover the delta function  $\delta(\mathbf{k} - \mathbf{k}')$ . When  $\mathbf{k} = \mathbf{k}'$  the integration over  $\mathbf{r}$  gives the volume  $\Omega$  occupied by the gas and the product  $\Omega \rho_i$  gives the number of target nucleons of type  $i$ . Therefore,

$$U_{FG}(\mathbf{k} = \mathbf{k}') = \delta_{\mu,\mu'} \delta_{\nu,\nu'} ( N_l \langle \boldsymbol{\kappa} | \mathbf{t}^0 + \mathbf{t}^1 | \boldsymbol{\kappa} \rangle_A + N_u \langle \boldsymbol{\kappa} | \mathbf{t}^0 - \mathbf{t}^1 | \boldsymbol{\kappa} \rangle_A ), \quad (17)$$

where  $N_l$  ( $N_u$ ) is the number of target nucleons like (unlike) the projectile. Similarly, the non-vanishing diagonal elements of the optical potential for charge-exchange reactions is

$$U_{FG}(\mathbf{k} = \mathbf{k}') = -2\sqrt{N-Z} \delta_{\mu-1,\mu'} \delta_{\nu,\nu'} \langle \boldsymbol{\kappa} | \mathbf{t}^1 | \boldsymbol{\kappa} \rangle_A. \quad (18)$$

If in Eq. (16), we use the local density approximation for  $\rho^{[i]}$  by allowing it to be a function of  $\mathbf{r}$ , then

$$U_{FG} = \delta_{\mu,\mu'} \delta_{\nu,\nu'} ( \tilde{\rho}_l(q) \langle \boldsymbol{\kappa} | \mathbf{t}^0 + \mathbf{t}^1 | \boldsymbol{\kappa} \rangle_A + \tilde{\rho}_u(q) \langle \boldsymbol{\kappa} | \mathbf{t}^0 - \mathbf{t}^1 | \boldsymbol{\kappa} \rangle_A ), \quad (19)$$

where  $\mathbf{q} = \mathbf{k} - \mathbf{k}'$ , the momentum transferred to the target and  $\tilde{\rho}_i$  is the Fourier transform of the density of nucleons of type  $i$ . This is an approximate form of the usual  $t\rho$  approximation to the optical potential.

## B. Scattering From Finite Nuclei

Results for finite nuclei may be obtained by expanding the creation and annihilation operators of Eq. (3) in a (spherical) shell-model basis. The result for arbitrary (allowed) spin and isospin transfer is

$$\left[ \psi_{\frac{1}{2}\frac{1}{2}}^\dagger(\mathbf{p}') \otimes \bar{\psi}_{\frac{1}{2}\frac{1}{2}}(\mathbf{p}) \right]^{SM;TN} = \sum_{nlj, n'l'j'} u_{nlj}(p) u_{n'l'j'}(p') \sum_{L,J} [\hat{L} \hat{J} \hat{j} \hat{j}' (-)^{l'+L+S+J}] \begin{pmatrix} l' & \frac{1}{2} & j' \\ l & \frac{1}{2} & j \\ L & S & J \end{pmatrix} \times$$

$$\{ [Y_{l'}(\hat{\mathbf{p}}') \otimes Y_l(\hat{\mathbf{p}})]^L \otimes [c_{n'l'j';\frac{1}{2}}^\dagger \otimes \bar{c}_{n'l'j';\frac{1}{2}}]^{J;TN} \}^{SM}, \quad (20)$$

where, in this equation,  $L, S, J, T$  denote transferred quanta  $L_t, T_t$  etc. Also,  $c^\dagger$  and  $\bar{c}$  denote creation operators for particles and holes, respectively, and  $u_{nlj}(p)$  is the radial part of a shell-model orbital in momentum space. The symbol in rounded parentheses is a nine-j symbol and  $\hat{x}$  denotes  $\sqrt{2x+1}$ . Inserting Eq. (20) into Eq. (7) gives the transition density for a finite nucleus

$$\rho_{FI}^{S_t T_t}(\mathbf{p}', \mathbf{p}) = 2 \sum_{nlj, n'l'j'} u_{nlj}(p) u_{n'l'j'}(p') \sum_{L_t J_t} [\hat{L}_t \hat{J}_t \hat{j} \hat{j}' (-)^{l'+L_t+S_t+J_t}] \begin{pmatrix} l' & \frac{1}{2} & j' \\ l & \frac{1}{2} & j \\ L_t & S_t & J_t \end{pmatrix} \times$$

$$\{ [Y_{l'}(\hat{\mathbf{p}}') \otimes Y_l(\hat{\mathbf{p}})]^{L_t} \otimes \langle F | [c_{n'l'j';\frac{1}{2}}^\dagger \otimes \bar{c}_{nlj;\frac{1}{2}}]^{J_t;T_t N_t} | I \rangle \}^{S_t M_t}. \quad (21)$$

Although only the  $S_t = 0$  part of the above density is required for the usual case of calculating the optical potential, it is useful to have the more general result for later use. For the special case in which the transferred quanta ( $L_t S_t J_t$ ) are either assumed or restricted to be zero, Eq. (21) becomes

$$\rho_{FI}^{T_t}(\mathbf{p}', \mathbf{p}) = \frac{-\sqrt{2}}{4\pi} \sum_{nlj} u_{nlj}(p) u_{nlj}(p') P_l(\hat{\mathbf{p}}' \cdot \hat{\mathbf{p}})$$

$$\sum_{\mu \nu \nu'} (-)^{\frac{1}{2}-\nu} \langle \frac{1}{2} \frac{1}{2} \nu' \nu | T_t N_t \rangle \langle F | c_{n'lj-\mu;\frac{1}{2}\nu'}^\dagger c_{nlj-\mu;\frac{1}{2}-\nu} | I \rangle. \quad (22)$$

For the special case of elastic scattering in which  $|F\rangle = |I\rangle$ ,  $n = n'$  and  $N = 0$ , the mixed density reduces to

$$\rho_{FI}^{T_t=1}(\mathbf{p}', \mathbf{p}) = \frac{1}{4\pi} \sum_{nlj} u_{nlj}(p) u_{nlj}(p') [Z_{nlj} + (-)^{T_t} N_{nlj}] P_l(\hat{\mathbf{p}}' \cdot \hat{\mathbf{p}}), \quad (23)$$



where  $Z_{nlj}$  and  $N_{nlj}$  denote the number of protons and neutrons in the state  $(nlj)$  where it has been assumed that the orbitals for neutrons and protons are the same. For the  $(p,n)$  charge-exchange reaction to the isobaric analogue state,  $\nu = \nu' = \frac{1}{2}$ ,  $T_t = N_t = 1$  and the Clebsch-Gordan coefficient is unity giving

$$\rho_{FI}^{T_t=1}(\mathbf{p}', \mathbf{p}) = -\sqrt{\frac{2}{N-Z}} \frac{1}{4\pi} \sum_{nlj} u_{nlj}(p) u_{nlj}(p') [N_{nlj} - Z_{nlj}] P_l(\hat{\mathbf{p}}' \cdot \hat{\mathbf{p}}). \quad (24)$$

From Eq. (6), the optical potential for elastic scattering associated with the transition density of Eq. (23) reduces to

$$U \rightarrow U_{pp,nn} = \delta_{\mu\mu'} \frac{1}{4\pi} \sum_{nlj} \int d\mathbf{p} u_{nlj}(p) u_{nlj}(p') P_l(\hat{\mathbf{p}}' \cdot \hat{\mathbf{p}}) \sum_{S_p=0,1} \frac{\langle \nu' | \mathbb{S}(S_p, \nu' - \nu) | \nu \rangle}{2S_p + 1} \times \\ (N_{nlj}^l \langle \boldsymbol{\kappa}' | \mathbf{t}^{S_p 0} + \mathbf{t}^{S_p 1} | \boldsymbol{\kappa} \rangle_A + N_{nlj}^u \langle \boldsymbol{\kappa}' | \mathbf{t}^{S_p 0} - \mathbf{t}^{S_p 1} | \boldsymbol{\kappa} \rangle_A), \quad (25)$$

where  $N_{nlj}^l$  and  $N_{nlj}^u$  denote the number of target nucleons in the state  $(nlj)$  which are like and unlike (isospin projection) the projectile and  $\mathbf{p}' = \mathbf{p} + \mathbf{q}$ . Similarly, the optical potential mediating the  $(p,n)$  reaction to the isobaric analogue of the target ground state is

$$U \rightarrow U_x = -\delta_{\mu-1,\mu'} \frac{2}{\sqrt{N-Z}} \frac{1}{4\pi} \sum_{nlj} \int d\mathbf{p} u_{nlj}(p) u_{nlj}(p') (N_{nlj} - Z_{nlj}) P_l(\hat{\mathbf{p}}' \cdot \hat{\mathbf{p}}) \\ \sum_{S_p=0,1} \frac{\langle \nu' | \mathbb{S}(S_p, \nu' - \nu) | \nu \rangle}{2S_p + 1} \cdot \langle \boldsymbol{\kappa}' | \mathbf{t}^{S_p 1} | \boldsymbol{\kappa} \rangle_A. \quad (26)$$

The above expressions can be further simplified in the case of non-spin transfer to the projectile. Denoting the proton and neutron mixed densities by  $\rho_p$  and  $\rho_n$ ,

$$\rho_p(\mathbf{p}', \mathbf{p}) = \sum_{nlj} u_{nlj}(p) u_{nlj}(p') Z_{nlj} P_l(\hat{\mathbf{p}}' \cdot \hat{\mathbf{p}}), \\ \rho_n(\mathbf{p}', \mathbf{p}) = \sum_{nlj} u_{nlj}(p) u_{nlj}(p') N_{nlj} P_l(\hat{\mathbf{p}}' \cdot \hat{\mathbf{p}}), \quad (27)$$

we are left with the following three terms to evaluate

$$U_{pp} = \frac{1}{4\pi} \int d\mathbf{p} [\rho_p(\mathbf{p}', \mathbf{p}) \langle \boldsymbol{\kappa}' | \mathbf{t}^0 + \mathbf{t}^1 | \boldsymbol{\kappa} \rangle_A + \rho_n(\mathbf{p}', \mathbf{p}) \langle \boldsymbol{\kappa}' | \mathbf{t}^0 - \mathbf{t}^1 | \boldsymbol{\kappa} \rangle_A], \\ U_x = \frac{-1}{2\pi\sqrt{N-Z}} \int d\mathbf{p} [\rho_n(\mathbf{p}', \mathbf{p}) - \rho_p(\mathbf{p}', \mathbf{p})] \langle \boldsymbol{\kappa}' | \mathbf{t}^1 | \boldsymbol{\kappa} \rangle_A, \\ U_{nn} = \frac{1}{4\pi} \int d\mathbf{p} [\rho_p(\mathbf{p}', \mathbf{p}) \langle \boldsymbol{\kappa}' | \mathbf{t}^0 - \mathbf{t}^1 | \boldsymbol{\kappa} \rangle_A + \rho_n(\mathbf{p}', \mathbf{p}) \langle \boldsymbol{\kappa}' | \mathbf{t}^0 + \mathbf{t}^1 | \boldsymbol{\kappa} \rangle_A]. \quad (28)$$

### C. *In-medium* calculations

The optical potential  $U_{pp}$ ,  $U_{nn}$  and  $U_x$  obtained in the previous section requires the convolution of single-particle wavefunctions with a two-body effective interaction. Simpler expressions for these potentials are obtained with the use of the Slater approximation to the ground-state mixed density in the case of spin-saturated targets. This approximation was examined in Ref. [13] in the context of nucleon elastic scattering at intermediate energies, and its effects are reported to be only noticeable at the larger scattering angles. Furthermore, this representation of the mixed density yields a simple prescription for including explicit medium effects by means of infinite nuclear matter  $g$  matrices. Following the same arguments discussed in Ref. [9] to incorporate nuclear medium effects, the first of the potentials expressed in Eqs. (28) takes the general form (c.f. Eq. (21) of Ref. [7])

$$U_{pp}(\mathbf{k}', \mathbf{k}) = \int d\mathbf{R} e^{i(\mathbf{k}' - \mathbf{k}) \cdot \mathbf{R}} [\rho_p(\mathbf{R}) \bar{g}_{pp}(\mathbf{k}', \mathbf{k}) + \rho_n(\mathbf{R}) \bar{g}_{np}(\mathbf{k}', \mathbf{k})] , \quad (29)$$

where  $\rho_p$  and  $\rho_n$  are the local proton and neutron point densities, respectively, and  $\bar{g}_{NN}$  represent off-shell Fermi-averaged amplitudes in the appropriate  $NN$  channel. More explicitly, in the context of infinite nuclear matter these density-dependent amplitudes are given by

$$\bar{g}_{NN}(\mathbf{k}', \mathbf{k}) = \frac{3}{4\pi \hat{k}^3} \int \Theta(\hat{k} - |\mathbf{P}|) g_{\mathbf{K}+\mathbf{P}}(\boldsymbol{\kappa}', \boldsymbol{\kappa}; \sqrt{s}; \bar{\rho}) d\mathbf{P} , \quad (30)$$

where  $g_{\mathbf{K}+\mathbf{P}}(\boldsymbol{\kappa}', \boldsymbol{\kappa}; \sqrt{s}; \bar{\rho})$  is taken as the  $g$  matrix for symmetric nuclear matter of density  $\bar{\rho}$ . Here,

$$\mathbf{K} = \frac{1}{2}(\mathbf{k} + \mathbf{k}') , \quad \mathbf{P} = \frac{1}{2}(\mathbf{p} + \mathbf{p}') , \quad \mathbf{k} + \mathbf{p} = \mathbf{k}' + \mathbf{p}' , \quad (31)$$

and the relativistically corrected relative momenta  $\boldsymbol{\kappa}$  and  $\boldsymbol{\kappa}'$  are given by

$$\boldsymbol{\kappa} = W\mathbf{k} - (1 - W)\mathbf{p} , \quad \boldsymbol{\kappa}' = W'\mathbf{k}' - (1 - W')\mathbf{p}' , \quad (32)$$

with  $W$  and  $W'$  scalar functions of the momenta of the colliding particles with relativistic kinematics built in [7]. Additionally, the local momentum  $\hat{k}$  is taken from  $\hat{k}^3 = 3\pi^2\bar{\rho}/2$ , with  $\bar{\rho} \rightarrow [\rho_p(R) + \rho_n(R)]/2$ , the isoscalar local density at radius  $R$ . Analogous expressions are obtained for  $U_x$  and  $U_{nn}$ .

### III. COUPLED-CHANNEL CALCULATIONS

Our study focuses on quasielastic scattering to the isobaric analog state. Considering explicitly the isospin degrees of freedom of the scattering waves in the form of outgoing

proton and neutron wavefunctions, we obtain a non-local version of the coupled-channel [14, 15] equations

$$\begin{bmatrix} \hat{K}_p + U_{pp}^{(s)} + V_C & U_x \\ U_x & \hat{K}_n + U_{nn} \end{bmatrix} \begin{pmatrix} \Psi_p \\ \Psi_n \end{pmatrix} = \begin{pmatrix} E_p \Psi_p \\ E_n \Psi_n \end{pmatrix}. \quad (33)$$

Here  $U_{nn}$  and  $U_x$  are the non-local potentials given by Eqs. (25) and (26) in the previous Section. Furthermore,  $U_{pp}^{(s)}$  represents the short-range coupling between the charged projectile and the target protons, i.e. the hadronic-plus-Coulomb contribution with the point-Coulomb potential,  $V_C = Ze^2/r$ , subtracted. A formal solution to these equations is given in the form of the Lippmann-Schwinger integral equation with proton waves  $\Phi_p$  in the entrance channel

$$\begin{pmatrix} \Psi_p \\ \Psi_n \end{pmatrix} = \begin{pmatrix} \Phi_p \\ 0 \end{pmatrix} + \begin{bmatrix} \mathcal{G}_p U_{pp}^{(s)} & \mathcal{G}_p U_x \\ \mathcal{G}_n U_x & \mathcal{G}_n U_{nn} \end{bmatrix} \begin{pmatrix} \Psi_p \\ \Psi_n \end{pmatrix}, \quad (34)$$

where  $\mathcal{G}_p$  and  $\mathcal{G}_n$  are the Green's functions for outgoing protons and neutrons, respectively. In coordinate space, for partial wave  $l$ , these propagators are expressed in terms of the Coulomb (and Bessel) spherical waves

$$\begin{aligned} \mathcal{G}_l^{(+)}(r, r'; k) &= -\frac{i}{k} \frac{2\bar{\epsilon}}{\hbar^2} F_l(\eta; kr_{<}) [F_l(\eta; kr_{>}) + iG_l(\eta; kr_{>})] \\ &\equiv -\frac{i}{k} \frac{2\bar{\epsilon}}{\hbar^2} F_l(\eta; kr_{<}) H_l^{(+)}(\eta; kr_{>}). \end{aligned} \quad (35)$$

Here  $\eta = Ze^2/\hbar v$ , represents the charge parameter for the  $NA$  coupling, with  $v$  the corresponding relative velocity, and  $\bar{\epsilon}$  the ejectile-residual nucleus reduced energy. For uncharged particles  $F_l$  and  $G_l$  become the usual Ricatti-Bessel functions with the following the phase conventions:  $F_l(0; t) = t j_l(t)$ ;  $j_0(t) = \sin t/t$ , and  $G_l(0; t) = t n_l(t)$ ;  $n_0(t) = -\cos t/t$ .

The primary input in these equations is the optical potential which we obtain following a current version of the full-folding OMP to nucleon scattering [7, 9]. In this scheme, the optical potential is calculated in momentum space leading to a general non-local structure in coordinate space, a feature which is retained throughout. An exact treatment of the Coulomb interaction in the presence of this non-local coupling is performed in coordinate space by solving Eq. (34) once the Fourier transform of the hadronic contribution have been performed. Thus, the scattering amplitude is readily obtained from the asymptotic behavior of the radial scattering waves from Eq. (34) which, schematically, has the form

$$\begin{bmatrix} u_{p,l}(r) \\ u_{n,l}(r) \end{bmatrix} \sim \begin{bmatrix} \frac{1}{k_p} F_l(\eta; k_p r) \\ 0 \end{bmatrix} + \begin{bmatrix} \Delta_{pp} \frac{1}{k_p} H_l^{(+)}(\eta; k_p r) \\ \Delta_{pn} \frac{1}{k_n} H_l^{(+)}(0; k_n r) \end{bmatrix}, \quad (36)$$

with  $k_p$  and  $k_n$  the momenta of the outgoing protons and neutrons, respectively. The above result provides alternative forms for obtaining the scattering amplitude, namely by simple identification of the asymptotic form of the solution, or by explicit evaluation of the matrix elements, i.e.

$$\begin{aligned}\Delta_{pp}^{(l)} &= \langle U_{pp}^{(s)} u_{p,l} + U_x u_{n,l} \rangle \equiv ik_p f_{pp}^{(l)}, \\ \Delta_{pn}^{(l)} &= \langle U_x u_{p,l} + U_{nn} u_{n,l} \rangle \equiv ik_n f_{pn}^{(l)}.\end{aligned}\tag{37}$$

More explicitly,

$$\langle U_{pp}^{(s)} u_{p,l} \rangle = -i \frac{2\bar{\epsilon}_p}{\hbar^2} \int_0^\infty dr \int_0^\infty dr' F_l(\eta; k_p r') [r' U_{pp}^{(s)}(r', r) r] u_{p,l}(r). \tag{38}$$

Analogous expressions hold for  $\langle U_{pn} u_{n,l} \rangle$  and  $\langle U_{nn} u_{n,l} \rangle$ .

The results obtained with this procedure were compared with DWBA results and showed almost unnoticeable differences.

#### IV. APPLICATIONS

The scattering calculations performed in this work differ from most reported applications of quasielastic nucleon exchange processes to date. Thus, it is important to spell out the differences explicitly. The optical potential is obtained *via* a convolution of the *in-medium* nuclear matter  $g$  matrix with the target ground state mixed density. We have considered six different  $NN$  potential models in the construction of the corresponding  $g$  matrix, i.e. the Paris potential [16], the Nijmegen I, Nijmegen II and Reid 93 potentials [17] the Argonne AV18 potential [18] and the charge-dependent Bonn potential [19]. The  $g$  matrix is calculated in momentum space fully off shell, evaluated at eight different densities and nearly twenty momentum pairs, for all allowed  $NN$  states up to  $J = 7$ , in a square mesh of relative momenta up to  $15 \text{ fm}^{-1}$ . The Fermi motion integrals involving the  $g$  matrix are made following Ref. [7], where relativistic kinematics at the  $NN$  level are included in the folding integrals, supplemented by a proper treatment of the deuteron pole contribution [20]. For simplicity, and in order to keep our discussion focused within a single scheme, we have restricted the use of the  $NN$  charge-dependent potential models to their  $NN T_z = 0$  components.

The results reported in this study are based on semi-phenomenological densities. Proton densities were obtained from parametrized charge densities [21], unfolding the electromagnetic proton size to obtain the corresponding point density. Neutron densities were obtained

by adding to the proton density a harmonic oscillator orbital of the form  $\psi \sim r^l e^{-a_n^2 r^2/2}$ . In the case of  $^{90}\text{Zr}$ , a 3pG charge density was used, with the neutron excess characterized by  $a_n=0.472 \text{ fm}^{-1}$ . This construction yields a proton (neutron) root-mean-square radius ( $R_{RMS}$ ) of 4.198 fm (4.363 fm). A similar construction was used for the  $^{48}\text{Ca}$  densities, with a 3pF charge density for the closed shells with the neutron excess characterized by  $a_n=0.524 \text{ fm}^{-1}$ . The resulting proton (neutron)  $R_{RMS}$  is 3.374 fm (3.580 fm). In the case of  $^{14}\text{C}$ , the proton density was represented by a modified harmonic oscillator. The neutron excess was characterized with  $a_n=0.510 \text{ fm}^{-1}$ . The proton (neutron)  $R_{RMS}$  is in this case 2.427 fm (2.611 fm). The scattering results obtained with these densities were consistent with a variety of choices for the neutron-excess wavefunctions.

### A. Results for $^{14}\text{C}(p,n)$

In Fig. 1 we present the measured [22] and calculated differential cross-section for the quasielastic  $^{14}\text{C}(p,n)$  reaction following the  $g$ -matrix approach described in the previous section. The excitation energy to the IAS,  $E_x$ , is 2.31 MeV [23].

In this figure, and also in Figs. 1, 2 and 4-7, we show results for the Paris (solid curves), CD-Bonn (dotted curves), Nijmegen I (short-dashed curves), Nijmegen II (long-dashed curves), Argonne AV18 (dot-dashed curves), and Reid-93 (dot-dot-dashed curves)  $NN$  potential models. Although in some cases the overlapping of the curves prevents their identification, this comparison allows one to visualize a moderate sensitivity of the calculated quantities to the choice of the  $NN$  model. Such is the case of Fig. 1, where the description of the differential cross section for scattering angles less than 25 degrees is reasonably well described by all  $NN$  potential models considered. A departure from the data is observed at larger angles, suggesting missing effects.

Another quantity of particular interest is the so-called Fermi cross section ( $\sigma_F$ ), that is to say, the forward-angle (zero-degree) differential cross section of the quasielastic  $(p,n)$  reaction. In Fig. 2 we present the measured and calculated Fermi cross sections for  $^{14}\text{C}(p,n)$ . The data are from Refs. [24, 25], and the various curves correspond to the six  $NN$  models considered. A note of caution should be kept in mind before interpreting this figure. Although the  $g$ -matrix full-folding optical model calculations account for relativistic kinematics, all the  $NN$  potential models have been developed for energies below pion production

threshold. Thus, the results in Fig. 2 above 350 MeV represent extrapolations of the  $NN$  models.

Below 150 MeV all  $NN$  models provide reasonably good descriptions of  $\sigma_F$ , albeit all of them underestimate the 80-MeV datum. As the energy increases, beginning at  $\sim 150$  MeV results using the Paris potential depart from the others, being followed by those using the CD-Bonn potential near 300 MeV. Above pion production threshold the CD-Bonn potential exhibits a distinctive uniform growth, being followed less strongly by the Nijmegen I and Reid-93 models. Over the whole energy range both the Argonne AV18 and Nijmegen II potentials yield results in closest agreement with the data. In contrast, the Paris potential exhibits qualitative differences from the other models, particularly the depth of its minimum near 300 MeV.

In a broad sense, the role of medium effects have been subject of significant interest in the description of  $NA$  processes. In Fig. 3 we contrast results for the Fermi cross section as function of the proton incident energy using the  $g$  matrix (solid curve) and  $t$  matrix (dashed curve). Here we also include results based on the off-shell  $t\rho$  approximation (dotted curve), a limiting case of the full-folding approach using the free  $t$  matrix and suppressing Fermi motion effects in the  $NN$  interaction. In all cases the Argonne AV18 potential is used. We observe that the differences between the  $g$ - and  $t$ -matrix approaches become more sizable at the lower energies. In general, the difference between the  $g$ - and  $t$ -matrix approaches above 150 MeV does not exceed 0.2 mb/sr, a useful upper bound of medium effects in  $(p,n)$  charge-exchange processes. At energies below 150 MeV the Fermi cross section exhibit sizable differences between both approaches.

## B. Results for $^{48}\text{Ca}(p,n)$ and $^{90}\text{Zr}(p,n)$

In addition to  $^{14}\text{C}(p,n)$ , we have also performed calculations for quasielastic nucleon charge-exchange scattering on  $^{48}\text{Ca}$  ( $E_x = 6.67$  MeV [23]) and  $^{90}\text{Zr}$  ( $E_x = 5.1$  MeV [26]) using the  $g$ -matrix full-folding approach. In Figs. 4 and 5 we present results for  $^{48}\text{Ca}(p,n)$  at 135 and 160 MeV (data taken from Ref. [27]), respectively. Similarly, in Figs. 6 and 7 we show results for  $^{90}\text{Zr}(p,n)$  at 120 (data taken from Ref. [26]) and 160 (data taken from Ref. [28]) MeV. The curve patterns follow the same convention as in Fig. 1.

In contrast to the  $^{14}\text{C}(p,n)$  case, the Fermi cross sections for these four applications are

significantly underestimated relative to the data. The calculated  $\sigma_F$  for  $^{48}\text{Ca}$  at 160 MeV averages  $2.6(\pm 0.1)$  mb/sr, considering the six  $NN$  potential models. At the same energy, but in the case of  $^{90}\text{Zr}$ , the average is  $1.7(\pm 0.1)$  mb/sr. The reported measurements for  $^{48}\text{Ca}$  and  $^{90}\text{Zr}$  are  $5.0\pm 0.3$  mb/sr and  $3.4\pm 0.4$  mb/sr, respectively, roughly twice as large as the calculated values. The measured-to-calculated ratio of  $\sigma_F$  at the lower energies increases to 2.3 ( $^{48}\text{Ca}$  at 135 MeV) and 3.0 ( $^{90}\text{Zr}$  at 120 MeV).

The results shown in Figs. 4-7 correspond to fully consistent coupled-channel results involving explicitly the diagonal ( $U_{pp}$  and  $U_{nn}$ ) and off-diagonal ( $U_x$ ) optical potentials based on the full-folding approach. Thus, they illustrate the degree of consistency among the three components of the potential within the theory. This is an important point to keep in mind, since it is possible to improve the description of the data with the use of the DWBA, supplemented by suitable phenomenological potentials for the  $nn$  channel. Indeed, in the upper frame of Fig. 8 we compare the differential cross section for proton scattering from  $^{90}\text{Zr}$  at 121 MeV. The elastic scattering data are from Ref. [29], the solid curve represents the full-folding OMP results and the sparse crosses a standard Woods-Saxon (WS) parametrization. Although the full-folding results are in superior agreement with the data over the whole angular range, the quality of both descriptions at angles below 25 degrees is comparable. A comparison at the hadronic level alone (i.e. suppressing the Coulomb term) is presented in the lower frame, where we show the differential cross section for *uncharged* nucleon scattering using the full-folding  $U_{pp}$  (solid curve),  $U_{nn}$  (dashed curve) and the local WS parametrization (sparse crosses). The similarity between the  $U_{pp}$  and  $U_{nn}$  is striking, suggesting their equivalence. The WS result is slightly larger than the other two cases.

In a DWBA application it is customary to use, for the scattered neutron wave,  $U_{nn} := U_{pp}$ . In Fig. 9 we compare the consistent coupled-channel full-folding OMP results (solid curve) with the corresponding DWBA results (dashed curves). In both cases we use the same  $U_x$  based on the full-folding OMP. However, for the DWBA application we use the parametric WS potential already described. The significant increase of the differential cross section over whole the angular range is clear.

In Fig. 10 we present the scattering amplitude ( $f$ ) as function of the angular momentum  $l$ . The upper and lower frame are for the real and imaginary components, respectively. The filled (open) circles corresponds to exact coupled-channel results extracted from Eqs.

(37) and (38), with the solid curves representing the sum of both contributions. The stars (\*) represent results based on DWBA using the full-folding  $x$  and  $nn$  couplings (DWBA-CC). The dashed curves correspond to DWBA calculations where the  $nn$  term has been replaced by a local WS parametrization (DWBA-WS). Clearly the imaginary component of the amplitude (lower frame) exhibits minor differences among the exact coupled-channel, DWBA-CC and DWBA-WS results. Additionally, we observe that the total amplitude is the result of a mutual cancellation of the  $U_x$  and  $U_{nn}$  contributions. In the upper frame for the real components, however, we notice major differences between DWBA-WS and either of the two coupled-channel applications. Indeed, the real part of the DWBA-WS amplitude is nearly twice as large as the other two. This difference is exclusively due to the nature of the diagonal coupling, extracted phenomenologically from other sources. In that sense, a phenomenological improvement of the data is achieved at the expense of a consistent two-channel description of the charge-exchange process.

The difficulties discussed above have been explored in the context of the neutron-to-proton relative distribution. We have investigated the discrepancy between the consistent coupled-channel  $g$ -matrix OMP results and the measured quantities by studying the sensitivity of the scattering observables to variations in the neutron density [30]. Preliminary results along this line suggest the presence of a neutron halo in the nuclear periphery, that is to say, pronounced ratio of the neutron to proton density away from the nuclear surface. A more thorough investigation of this fact is a natural extension of the present work, and should not be limited to the radial matter distribution but include other features of the mixed density as well. An additional element in this discussion is the charge-dependence of the  $NN$  interaction, which in this work, has only been included in the  $T_z = 0$   $NN$  sector.

### C. Comparison with other results

Various microscopic studies on  $(p,n)$  charge-exchange reactions have been presented in the past. The most recent one by Bauge *et al.* [31] consists of a Lane-consistent semi-microscopic optical model approach where an energy-dependent potential depth normalization factor is applied to the isovector components. These normalization factors are then used consistently in elastic and quasielastic scattering. Their quasielastic charge-exchange applications between 100 and 200 MeV exhibit less pronounced discrepancies with the data relative to the



ones presented in this work. A microscopic extraction of these scaling factors remains to be seen.

A relativistic description of  $(p,n)$  quasielastic reactions has also been provided by Clark *et al.* [12]. In their case the relativistic impulse approximation is used, where Lorentz vector and scalar, isovector and isoscalar  $NA$  optical potentials are obtained from invariant  $NN$  amplitudes. Applications at 160 MeV for  $^{90}\text{Zr}(p,n)$  lead to a Fermi cross section weaker by a factor of 2 relative to the data. Their interpretation is that the diagonal optical potential presents too much absorption. A sizable improvement in the description of the differential cross section is obtained with the use of phenomenological (diagonal) potentials in conjunction with DWBA.

Although both approaches provide means by which to improve the description of the data, they also emphasize the limited understanding of this very simple process.

## V. SUMMARY AND CONCLUSIONS

We have studied quasielastic  $(p,n)$  charge-exchange reactions to the IAS at proton energies between 80 and 800 MeV. The study is based on an extension of the microscopic full-folding optical model approach for  $NA$  elastic scattering to processes where spin and isospin excitations become allowed. Thus, we have developed the necessary spin-isospin recoupling in order to identify the off diagonal terms responsible for the exchange mechanism. In this particular work we focus on isospin excitations only. The resulting couplings, in the form of non-local optical potentials, are then applied to quasielastic  $(p,n)$  reactions on  $^{14}\text{C}$ ,  $^{48}\text{Ca}$  and  $^{90}\text{Zr}$  at intermediate proton energies. Emphasis is given to the full consistency of the microscopic approach, without resorting to the use of adjusting parameters of the model in order to describe the data. Indeed, it has been a primary focus of this work to disclose its limitations in its most complete current form, *i.e.* with an accurate account of the Fermi motion (off shell), and implied non localities in the optical potentials. Exact coupled-channel calculations, within numerical accuracy, were performed to obtain the scattering observables. Comparisons with the data show a persistent deficiency of the theory to account for them in a consistent fashion. This is particularly so in the case of the heavier targets, where the zero-degree Fermi cross sections are substantially underestimated. We observe, however, that the use of phenomenological representations of the optical potential

for the elastic channel yields sizable changes of the Fermi cross sections. However, this phenomenological correction does not allow a clear identification of the missing microscopic effects needed to account for the data.

The above mentioned limitations become less dramatic in the case of  $(p,n)$  charge-exchange reactions on  $^{14}\text{C}$ . In this case the full-folding optical model approach is able to explain reasonably well the differential cross section at 120 MeV. Additionally, depending on the  $NN$  potential model, the Fermi cross section is described with varying degrees of success in the energy range 80-800 MeV. These applications represent extrapolations of the of the underlying  $NN$  potential model and favor the Nijmegen II and Argonne AV18 models. A more definitive assessment of such results would require, however, the account for the above-threshold inelasticities at the  $NN$  level, an issue to be considered in the future.

Though this work represents the most complete microscopic calculations to date, accounting for full Fermi motion effects and implied non localities, with an accurate treatment of the resulting coupled-channel reaction equations, we conclude that the model is still unable to satisfactorily describe the data. The discrepancies are not minor, especially in the cases of  $(p,n)$  reactions on  $^{48}\text{Ca}$  and  $^{90}\text{Zr}$  studied here, where the zero-degree Fermi cross section is underestimated by factors of 2 or 3. Although the data can be described by using distorted waves based on phenomenological optical models, or by adjusting other parameters of the model, we have preferred to maintain the formal structure of the theory to stress the limitations of the microscopic model in its current form. There are other venues for the inclusion of additional effects not discussed here. Among the most immediate ones we mention the role of asymmetric nuclear matter in the  $NN$  effective interaction and the neutron distribution in the target ground state [30]. Work toward inclusion of isospin asymmetry in the effective interaction is under way.

## Acknowledgments

The authors thank Prof. Jacob Rapaport for his kindness in providing available charge-exchange data. H. F. A. thanks the hospitality of the Department of Physics and Astronomy of the University of Georgia during his visit in the course of this collaboration. Partial funding for this work has been provided by FONDECYT under Grant No 1040938.

- 
- [1] Bao-An Li, Pawel Danielewicz, and William G. Lynch, Phys. Rev. C 71, 054603 (2005).
  - [2] E. N. E. van Dalen, C. Fuchs, and Amand Faessler, Phys. Rev. C 72, 065803 (2005).
  - [3] Jian Rong, Zhong-Yu Ma, and Nguyen Van Giai, Phys. Rev. C 73, 014614 (2006).
  - [4] J. R. Stone, P. D. Stevenson, J. C. Miller, and M. R. Strayer, Phys. Rev. C 65, 064312 (2002).
  - [5] H. Scheit, F. Maréchal, T. Glasmacher, E. Bauge, Y. Blumenfeld, J. P. Delaroche, M. Girod, R. W. Ibbotson, K. W. Kemper, J. Libert, B. Pritychenko, and T. Suomijärvi, Phys. Rev. C 63, 014604 (2001).
  - [6] R. Nojarov, Phys. Rev. C 54, 668 (1996).
  - [7] H. F. Arellano and H. V. von Geramb, Phys. Rev. C 66, 024602-1 (2002).
  - [8] H. F. Arellano, F. A. Brieva, and W. G. Love, Phys. Rev. Lett. 63, 605 (1989).
  - [9] H. F. Arellano, F. A. Brieva, and W. G. Love, Phys. Rev. C 52, 301 (1995).
  - [10] K. Amos, P. J. Dortmans, H. V. von Geramb, S. Karataglidis, and J. Raynal, Adv. in Nucl. Phys. 25 (2000) 275.
  - [11] Taksu Cheon and Kazuo Takayanagi, Phys. Rev. Lett. 68, 1291 (1992).
  - [12] B. C. Clark, S. Hama, E. Sugarbaker, M. A. Franey, R. L. Mercer, L. Ray, G. W. Hoffmann, and B. D. Serot, Phys. Rev. C 30, 314 (1984).
  - [13] H.F. Arellano, F.A. Brieva and W.G. Love, Phys. Rev. C 42, 652 (1990).
  - [14] A. M. Lane, Nucl. Phys. 35, 676 (1962).
  - [15] G. W. Hoffmann, Phys. Rev. C 8, 761 (1973).
  - [16] M. Lacombe, B. Loiseau, J. M. Richard, and R. Vinh Mau, J. Côté, P. Pirés and R. de Tourreil, Phys. Rev. C 21, 861 (1980).
  - [17] V. G. J. Stoks, R. A. M. Klomp, C. P. F. Terheggen, and J. J. de Swart, Phys. Rev. C 49, 2950 (1994).
  - [18] R. B. Wiringa, V. G. J. Stoks, and R. Schiavilla, Phys. Rev. C 51, 38 (1995).
  - [19] R. Machleidt, Phys. Rev. C 63, 024001 (2001).
  - [20] H. F. Arellano, F. A. Brieva, and W. G. Love, Phys. Rev. C 50, 2480 (1994).
  - [21] C. W. de Jager, H. de Vries, and C. de Vries, At. Data Nucl. Data Tables 14, 479 (1974).
  - [22] Jacob Rapaport, unpublished (private communication).
  - [23] B. D. Anderson, M. Mostajabodda'vati, C. Lebo, R. J. McCarthy, L. Garcia, J. W. Watson,

- and R. Madey, Phys. Rev. C 43, 1630 (1991).
- [24] T. N. Taddeucci, J. Rapaport, D. E. Bainum, C. D. Goodman, C. C. Foster, C. Gaarde, J. Larsen, C. A. Goulding, D. J. Horen, T. Masterson, and E. Sugarbaker, Phys. Rev. C 25, 1094 (1982), and references therein.
  - [25] E. Sugarbaker, D. Marchlinski, T. N. Taddeucci, L. J. Rybarcyk, J. B. McClelland, T. A. Carey, R. C. Byrd, C. D. Goodman, W. Huang, J. Rapaport, D. Mercer, D. Prout, W. P. Alford, E. Gülmez, C. A. Whitten, and D. Ciskowski, Phys. Rev. Lett. 65, 551 (1990).
  - [26] D. E. Bainum, J. Rapaport, C. D. Goodman, D. J. Horen, C. C. Foster, M. B. Greenfield, and C. A. Goulding, Phys. Rev. Lett. 44, 1751 (1980).
  - [27] B. D. Anderson, T. Chittrakarn, A. R. Baldwin, C. Lebo, R. Madey, P. C. Tandy, J. W. Watson, B. A. Brown, and C. C. Foster, Phys. Rev. C 31, 1161 (1985).
  - [28] E. Sugarbaker *et al.*, Proceedings of the International Conference on Nuclear Structure, Amsterdam, 1982, edited by A. Van Der Wonde and B. J. Verhaar, pp. 77. Jacob Rapaport (private communication).
  - [29] Alan Scott (unpublished).
  - [30] H. F. Arellano and W. G. Love, Nucl. Phys. A 755C, 527 (2005).
  - [31] E. Bauge, J. P. Delaroche, and M. Girod, Phys. Rev. C 63, 024607 (2001)

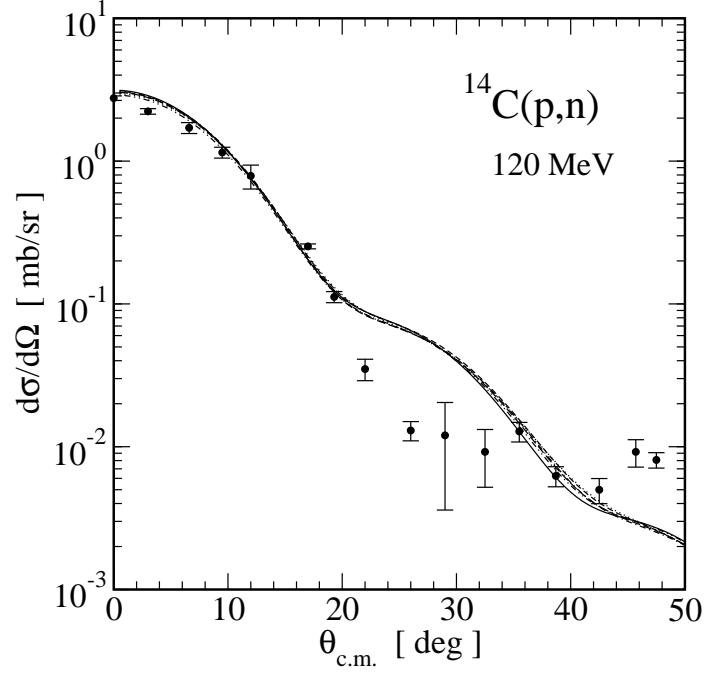


FIG. 1: Measured [22] and calculated differential cross-section for  $^{14}\text{C}(p,n)$  at 120 MeV. For reference to the curves see the text.

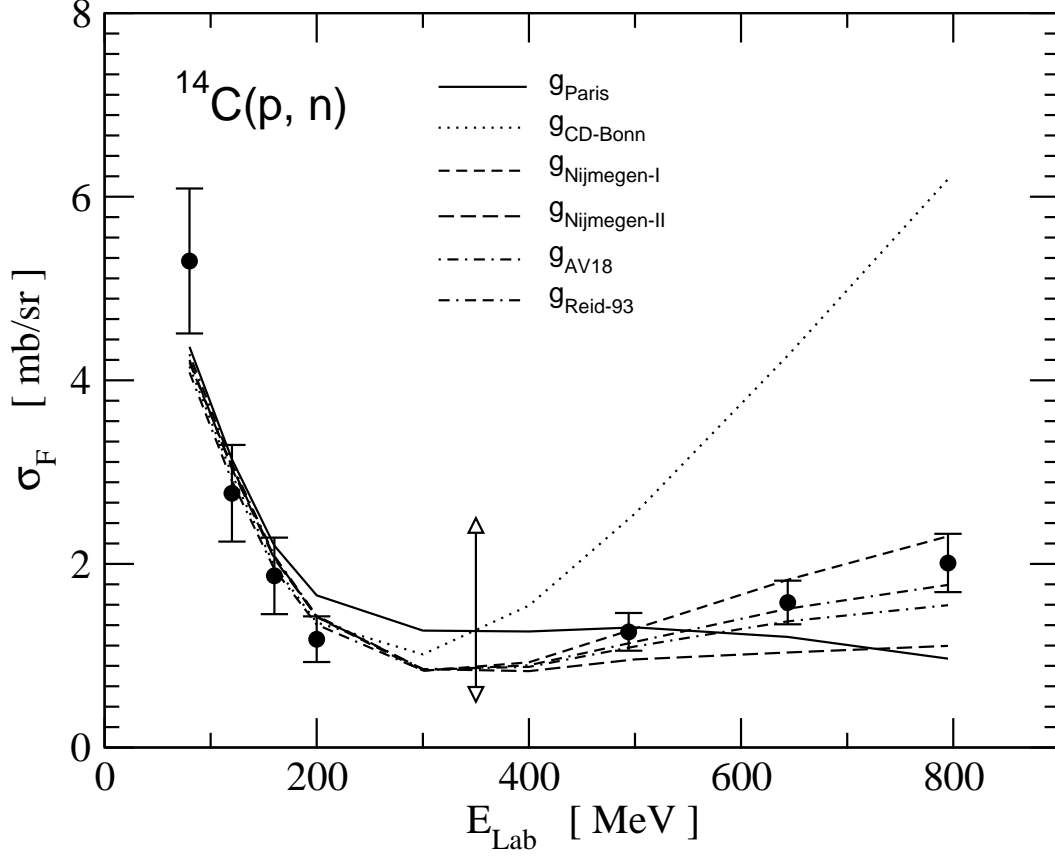


FIG. 2: The zero-degree Fermi cross section based on  $g$ -matrix full-folding optical model potentials using different  $NN$  potential models. For reference to the data see text. The dashed line at 350 MeV indicates the energy from which the calculations should be taken as extrapolations of all  $NN$  models.

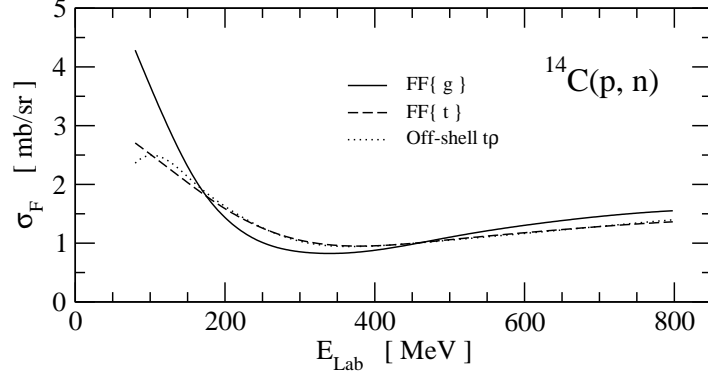


FIG. 3: The zero-degree Fermi cross section based on full-folding OMP using the  $g$  matrix (solid curve) and  $t$  matrix (dashed curve). Off-shell  $t\rho$  results are represented with the dotted curve. All three results use the Argonne AV18  $NN$  potential.

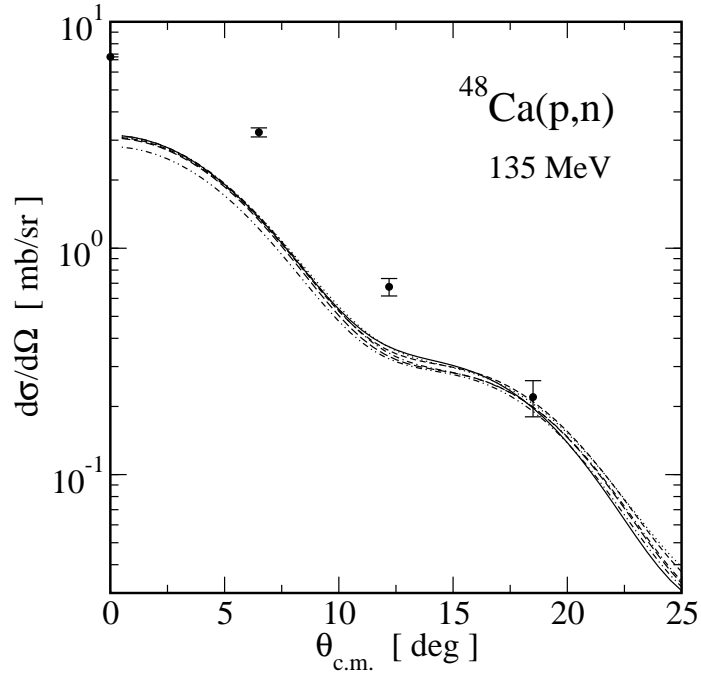


FIG. 4: Measured [23] and calculated differential cross-section for  $^{48}\text{Ca}(p, n)$  at 135 MeV. The curve patterns follow the same convention as in Fig. 2.

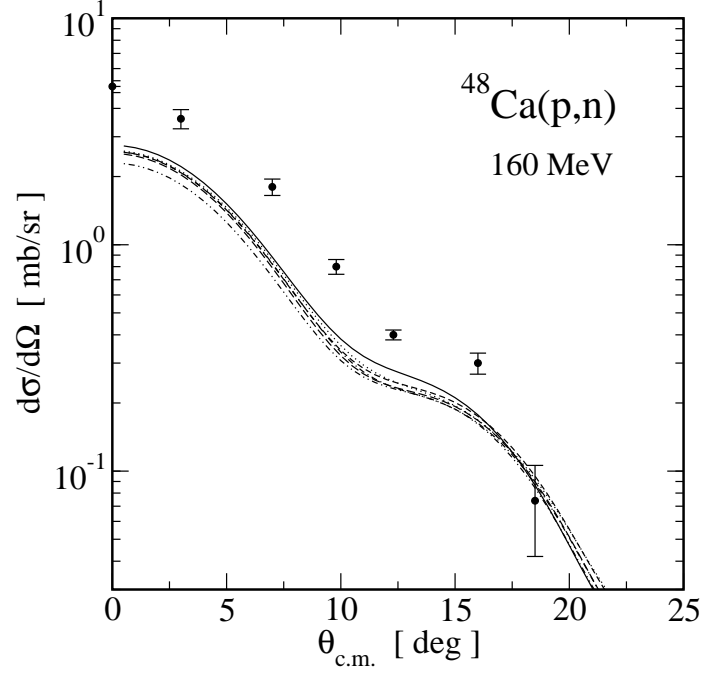


FIG. 5: Measured [27] and calculated differential cross-section for  $^{48}\text{Ca}(p,n)$  at 160 MeV. The curve patterns follow the same convention as in Fig. 2.

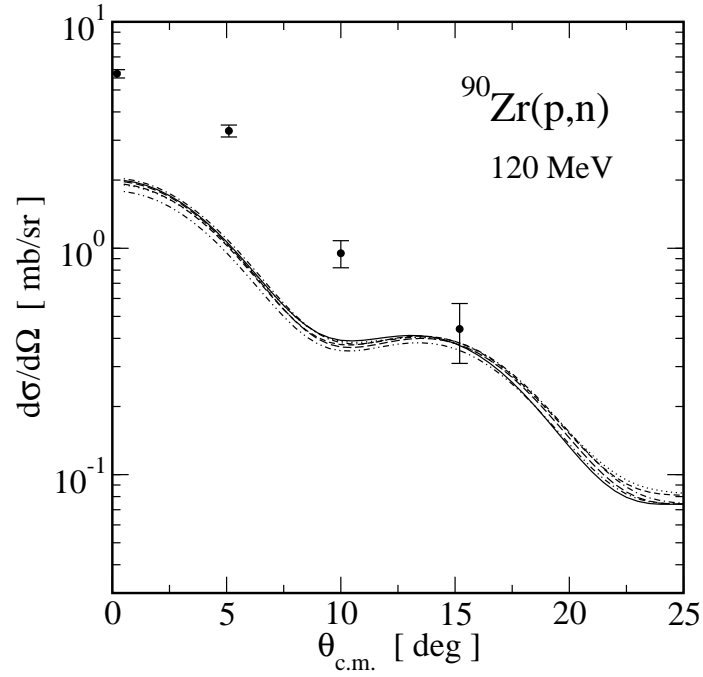


FIG. 6: Measured [26] and calculated differential cross-section for  $^{90}\text{Zr}(p,n)$  at 120 MeV. The curve patterns follow the same convention as in Fig. 2.



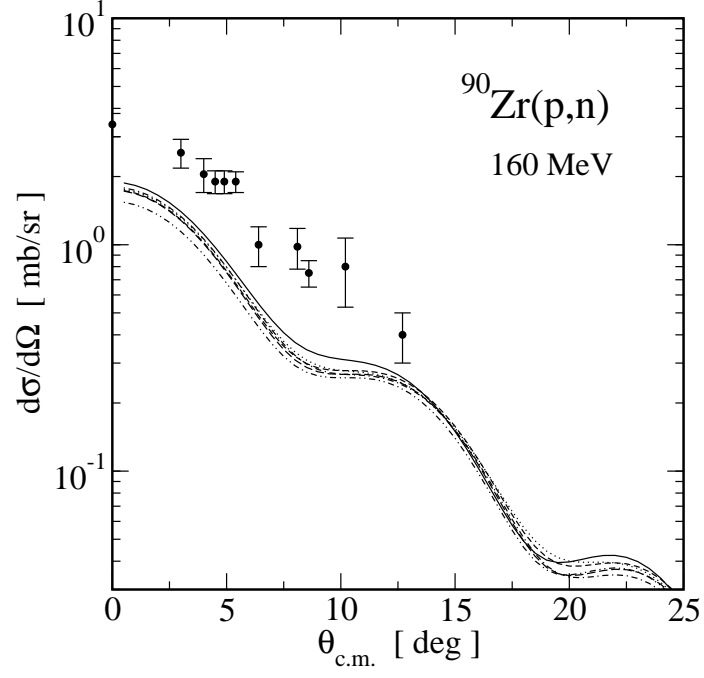


FIG. 7: Measured [28] and calculated differential cross-section for  $^{90}\text{Zr}(p,n)$  at 160 MeV. The curve patterns follow the same convention as in Fig. 2.

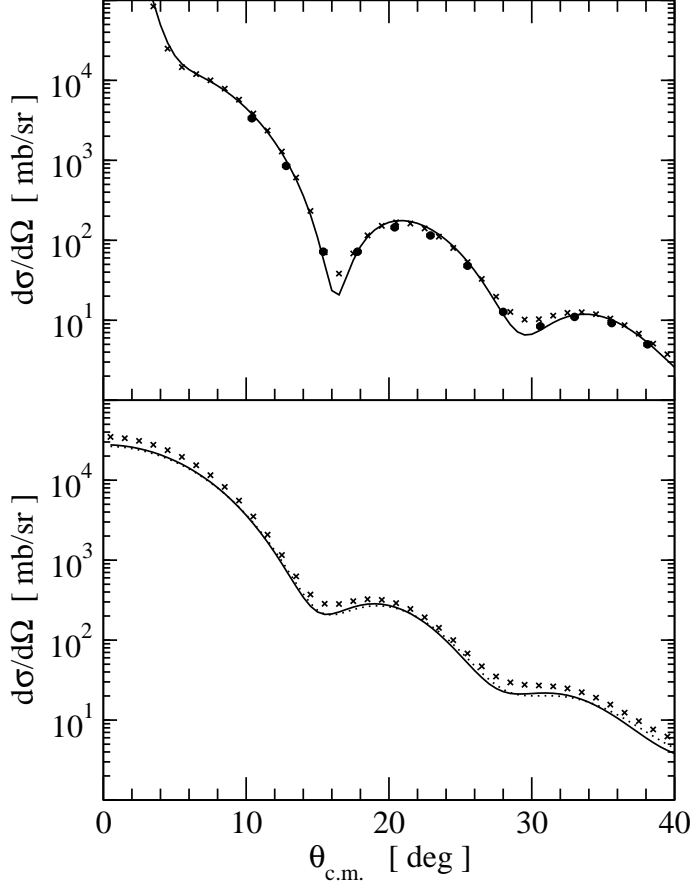


FIG. 8: Upper frame: Measured [29] and calculated differential cross-section for proton elastic scattering from  $^{90}\text{Zr}$  at 121 MeV. The solid curve corresponds to  $g$ -matrix full-folding OMP results, whereas the crosses correspond to a local WS parametrization. Lower frame: The calculated *uncharged* nucleon differential cross-section based on  $U_{pp}$  (solid curve),  $U_{nn}$  (dotted curve) and the WS parametrization (sparse crosses).

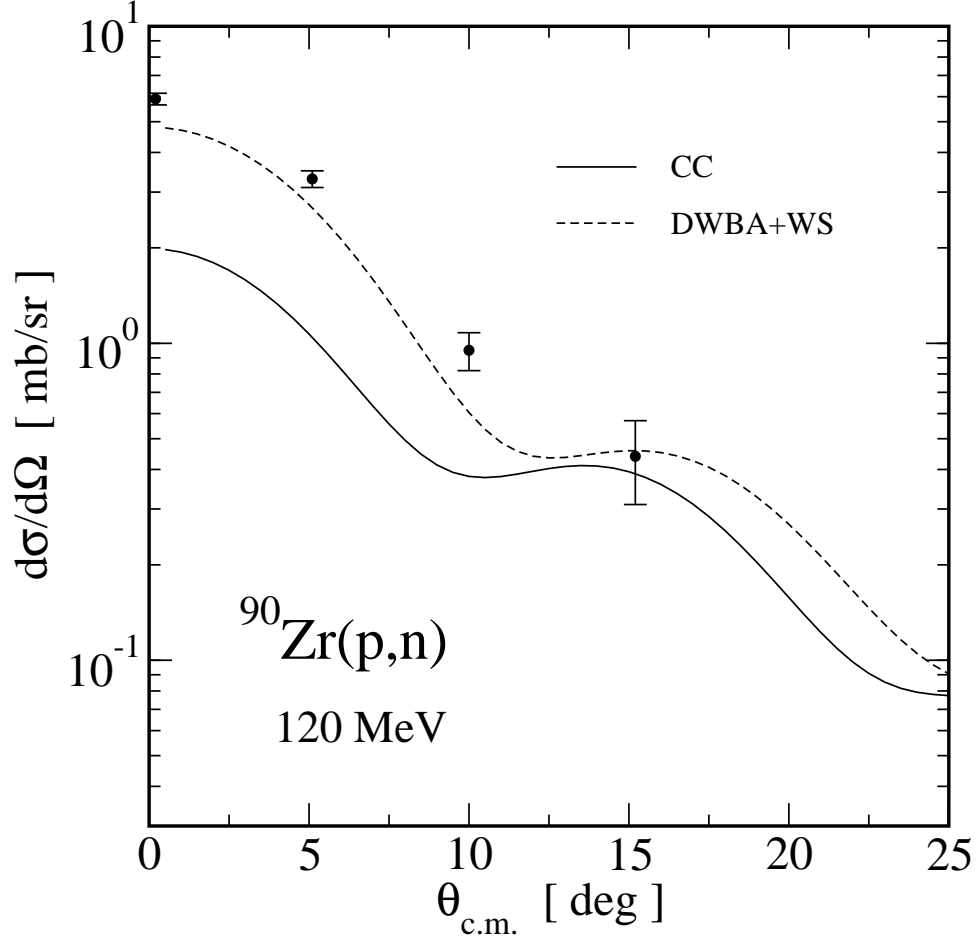


FIG. 9: Measured [26] and calculated differential cross section for  $^{90}\text{Zr}(p,n)$  charge-exchange reaction based on full coupled-channel (solid curve) and DWBA using the parametric WS potential (dashed curve).

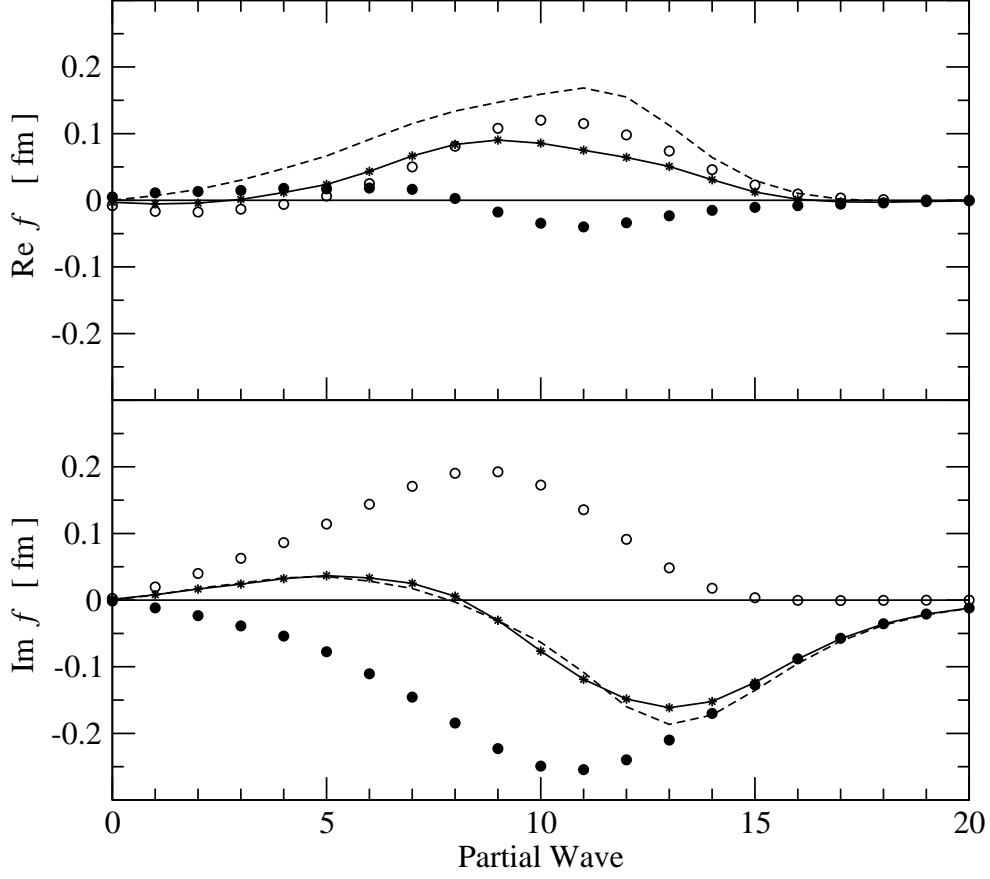


FIG. 10: The real (upper frame) and imaginary (lower frame) component of the scattering amplitude  $f$  as function of the orbital angular momentum. The solid curves, \* symbols and dashed curves represent the exact CC, DWBA-CC and DWBA-WS results, respectively. The filled and empty circles represent the  $U_x$  and  $U_{nn}$  contributions to the total amplitude [c.f. Eq. (37)].